International Journal of General Medicine

Dovepress
Taylor & Francis Group

Open Access Full Text Article

ORIGINAL RESEARCH

AI-Assisted Compressed Sensing Enables Faster Brain MRI for the Elderly: Image Quality and Diagnostic Equivalence with Conventional Imaging

Wenquan Gu[1,*], Chunhong Yang[1,*], Yuhui Wang[2], Wentao Hu[3], Dongmei Wu[4], Sunmei Cai[1], Guoxiong Hong[1], Peng Hu[5], Qi Zhang[1], Yongming Dai[5]

[1]Department of Radiology, Shanghai Punan Hospital of Pudong New Area, Shanghai, People's Republic of China; [2]Department of Neurology, Shanghai Punan Hospital of Pudong New Area, Shanghai, People's Republic of China; [3]Department of Radiology, Renji Hospital, School of Medicine, Shanghai Jiao Tong University, Shanghai, People's Republic of China; [4]Shanghai Key Laboratory of Magnetic Resonance, East China Normal University, Shanghai, People's Republic of China; [5]School of Biomedical Engineering & State Key Laboratory of Advanced Medical Materials and Devices, ShanghaiTech University, Shanghai, People's Republic of China

*These authors contributed equally to this work

Correspondence: Yongming Dai, School of Biomedical Engineering & State Key Laboratory of Advanced Medical Materials and Devices, ShanghaiTech University, Shanghai, People's Republic of China, Tel/Fax +86 21 20685265, Email dymdym118@163.com; Qi Zhang, Department of Radiology, Shanghai Punan Hospital of Pudong New Area, Shanghai, People's Republic of China, Tel/Fax +86 21 20302000, Email 18918070996@189.cn

Purpose: Conventional brain MRI protocols are time-consuming, which can lead to patient discomfort and inefficiency in clinical settings. This study aims to assess the feasibility of using artificial intelligence-assisted compressed sensing (ACS) to reduce brain MRI scan time while maintaining image quality and diagnostic accuracy compared to a conventional imaging protocol.

Patients and Methods: Seventy patients from the department of neurology underwent brain MRI scans using both conventional and ACS protocols, including axial and sagittal T2-weighted fast spin-echo sequences and T2-fluid attenuated inversion recovery (FLAIR) sequence. Two radiologists independently evaluated image quality based on avoidance of artifacts, boundary sharpness, visibility of lesions, and overall image quality using a 5-point Likert scale. Pathological features, including white matter hyperintensities, lacunar infarcts, and enlarged perivascular spaces, were also assessed. The interchangeability of the two protocols was determined by calculating the 95% confidence interval (CI) for the individual equivalence index. Additionally, Cohen's weighted kappa statistic was used to assess inter-protocol intra-observer agreement.

Results: The ACS images demonstrated superior quality across all qualitative features compared to the conventional ones. Both protocols showed no significant difference in detecting pathological conditions. The 95% CI for the individual equivalence index was below 5% for all variables except enlarged perivascular spaces, indicating the interchangeability of the conventional and ACS protocols in most cases. The inter-rater reliability between the two radiologists was strong, with kappa values of 0.78, 0.74, 0.70 and 0.86 for image quality evaluation and 0.74, 0.80 and 0.70 for diagnostic performance, indicating good-to-excellent agreement in their evaluations.

Conclusion: The ACS technique reduces brain MRI scan time by 29.2% while achieving higher image quality and equivalent diagnostic accuracy compared to the conventional protocol. This suggests that ACS could be potentially adopted for routine clinical use in brain MRI.

Keywords: brain, magnetic resonance imaging, fast imaging, deep learning, compressed sensing

Introduction

Prevalence of age-related cerebral diseases, such as neurodegenerative diseases and cerebrovascular diseases, inevitably increases in the context of the extending human life expectancy.[1] MRI plays a crucial role in diagnosing neurological conditions in aging populations.[2–4] For example, the diagnosis of cerebrovascular disease heavily relies on the size, number and position of the abnormalities seen on MRI, including white matter hyperintensities (WMH), infarcts and

Received: 4 November 2024
Accepted: 18 January 2025
Published: 23 January 2025

perivascular spaces.[5] Such features are also informative for degenerative diseases like multiple sclerosis or Alzheimer's disease.[6,7] However, MRI struggles with its inherent limitations in temporal and spatial resolution. These limitations lead to longer scan time, which can cause both occurrence of unexpected motion artifacts for diagnosis, and uncomfortable experience for elderly ones.[8] Moreover, extended examination duration, meaning high equipment usage and staffing costs, leads to raised economic burden,[9] and finally worsen MRI accessibility for the whole community.

To address these issues, accelerated imaging techniques such as Parallel Imaging (PI) and Compressed Sensing (CS) have been developed over the years.[10–12] K-space, or Fourier space, is the domain where the raw MRI signal data, along with spatial encoding information, are represented. It is derived by applying Fourier transformation to the spatial domain. PI, introduced decades ago, utilizes multiple receiver coils to simultaneously collect MRI data, enabling faster scan times by leveraging the combined sensitivity and spatial information from each coil.[11] While PI accelerates scan speed, it often compromises image quality as acceleration factors increase.[11] Even with PI, a typical 3.0 T brain MRI examination still takes 5–10 minutes, with additional time required for contrast-enhanced imaging. In contrast, CS, which has been clinically applied for over a decade, provides a new approach by recovering imaging data from under-sampled k-space through the exploitation of sparsity.[13] Using incoherent sampling, CS acquires a limited number of signals, which are then reconstructed with high probability via advanced algorithms, ultimately yielding higher-quality images through Fourier transform.[13] CS enhances speed while preserving image quality, though its effectiveness depends on specific conditions and the sparsity of the image data.[13,14]

In recent years, artificial intelligence (AI) emerges as a promising tool for further solving these problems. The AI solutions can be categorized into two groups: k-space reconstruction and image-based post-processing. For example, patch-based iterative image reconstruction, a method of image-based post-processing, has demonstrated efficacy in denoising.[15] In contrast, AI-based k-space reconstruction operates directly on raw k-space data during the scan and integrates more effectively with established accelerating techniques like PI and CS.[16] After training, neural networks can leverage prior knowledge of anatomical similarities to reconstruct high-quality images with reduced k-space acquisition.[16] Artificial intelligence-assisted compressed sensing (ACS) is one such techniques.[17] By integrating AI with traditional acceleration methods, ACS aims to reduce scan time while maintains the image quality.[17] Early studies in liver and kidney imaging suggest that ACS could improve patient compliance and diagnostic outcomes, though further validation is needed.[18,19] The application of ACS in brain imaging remains limited. As noted, common cerebral abnormalities such as white matter degeneration, infarcts, and perivascular spaces are prevalent in elderly individuals and require frequent structural brain MRIs. Evaluating both image quality and diagnostic utility of ACS is crucial for improving neuroimaging efficiency, particularly for managing the growing elderly population in low- and middle-income countries with limited access to advanced imaging technologies.

This study aims to evaluate the effectiveness of ACS in neuroimaging for aging patients. We compared ACS with conventional T2-weighted and T2-FLAIR MRI images using PI, focusing on both image quality and diagnostic utility. Our goal was to determine if ACS can overcome the specific challenges of neuroimaging in elderly patients for long scan time and head motion artifacts.

Materials and Methods

Participants

This prospective study was approved on January 17th 2023 by the local ethics committee of Shanghai Punan hospital of Pudong new area (PN2022002), and written informed consent was obtained for all patients. The study followed the ethical principles of the 1975 Declaration of Helsinki, as revised in 2013, for all procedures involving human subjects. Between January and June 2024, a total of 82 individuals were consecutively recruited from the department of neurology at our hospital for brain MRI examinations. Participants were excluded by the radiologist (WG, with 6 years of experience) if they were younger than 50 years, did not have a complete brain MRI scan, or if excessive motion artifacts rendered the MRI scans non-diagnostic. As a result, 70 patients were included in our study (Figure 1). For each participant, we collected demographic and clinical data, along with MRI data.

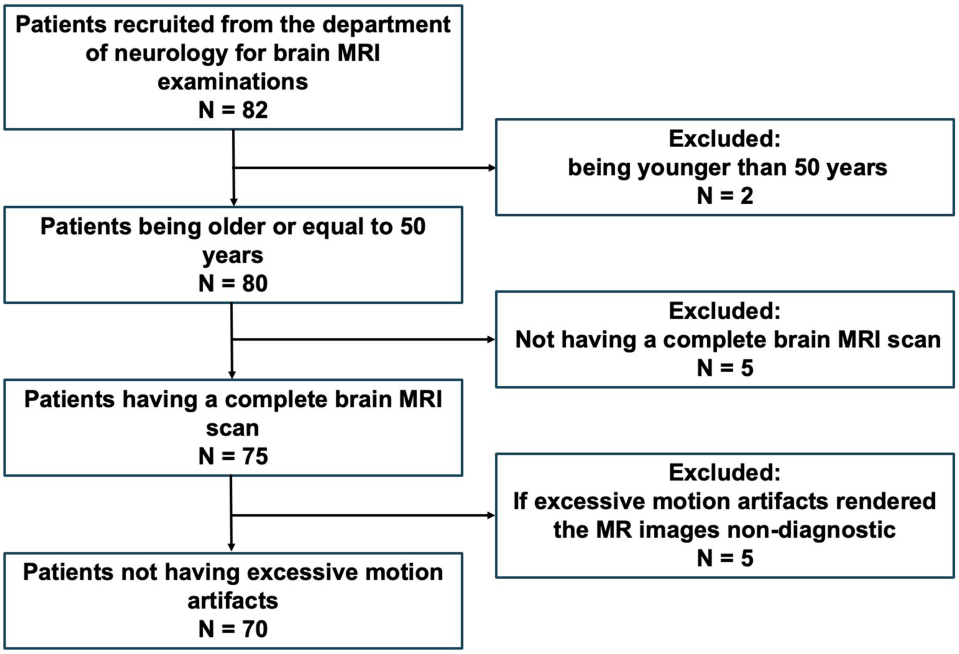

Figure 1 Flowchart of the patient exclusion process.

Image Acquisition

Brain MRI examinations were performed using a 3.0 Tesla MRI scanner (uMR870, United Imaging Healthcare, Shanghai, China), equipped with a commercial 24-channel head-neck coil. Each participant underwent both the conventional and ACS protocols, which included axial and sagittal T2-weighted fast spin-echo sequences, as well as T2-fluid attenuated inversion recovery (FLAIR) sequence. We implemented a conventional sequence first and then the corresponding ACS one. Importantly, the imaging parameters – such as repetition time (TR), echo time (TE), and echo train length – used in the ACS sequences were consistent with those employed in the conventional sequences for the same participant. The total acquisition time of the ACS protocols was 2 minutes 43 seconds, compared to 3 minutes 50 seconds for the conventional protocols. Table 1 summarizes the detailed MRI protocols included for comparison. For part of the

Table 1 Acquisition Parameters and Scan Times for Conventional and ACS Protocols

Sequence	Conventional	ACS	Conventional	ACS	Conventional	ACS
	Axial T2WI (FSE)		Sagittal T2WI (FSE)		Axial T2-FLAIR (FSE)	
TR/TE (ms)	6225/141	6225/1442	4600/109	4600/112	8000/125	8000/126
Flip angle (°)	90	90	110	110	150	150
Inverse Time (ms)	/	/	/	/	2415	2415
Field of view (mm)	230 x 200	230 x 200	230 x 200	230 x 200	230 x 200	230 x 200
Slices	21	21	21	21	21	21
Acquisition Matrix	384 x 301	384 x 301	336 x 302	336 x 302	288 x 213	288 x 213
Thickness / Gap (mm)	5.0 / 1.5	5.0 / 1.5	5.0 / 1.5	5.0 / 1.5	5.0 / 1.5	5.0 / 1.5
Echo train length	28	28	22	22	34	34
Number of averages	1.5	1.5	1.3	1.3	1.1	1.1
Acceleration factor	2	2.2	2	2.2	2	2.2
Scan time (min:s)	1:15	0:53	1:08	0:48	1:27	1:02
Total scan time (min:s)	Conventional: 3:50			ACS: 2:43		

Abbreviations: ACS, artificial intelligence-assisted compressed sensing; FLAIR, fluid attenuated inversion recovery; FSE, fast spin echo; TE, echo time; TR, repetition time; WI, weighted image.

https://doi.org/10.2147/IJGM.S499950

patients, other brain MRI sequences were scanned, including T1-weighted images, diffusion-weighted images or susceptility-weighted images, respectively, according to clinical request while not included for this study. These sequences were performed after those included in the study.

AI-Assisted Acceleration

ACS is a vendor-provided accelerating technique with FDA approval (United Imaging Healthcare, Shanghai, China) that leverages deep learning to enhance CS.[13] This approach incorporates an AI module powered by deep neural networks, designed to learn the distinctive features of high-quality, fully sampled images free of reconstruction artifacts. The AI module transforms the acquired full k-space data into the desired image space output. Trained using a Residual Neural Network (ResNet) architecture,[20] which is commonly used in Convolutional Neural Networks (CNNs), the network consists of two convolutional layers and a skip connection, with an additional long skip connection between the input and output. This structure accelerates learning by capturing the residual differences between fully sampled and under-sampled images. To further improve image quality, a least-squares generative adversarial network (GAN) training strategy is employed.[18] Figure 2 illustrates the network design.[21,22] In this process, the under-sampled images captured during the scan serve as the genuine data, while the Data Consistency Checking model within the network ensures accuracy by maintaining the integrity of the data throughout the reconstruction process.

Approximately two million fully sampled MR images, covering multiple human body parts including the brain and free from reconstruction artifacts, were used as the ground truth for training. These images, sourced from both phantoms (2%) and volunteers (98%), were retrospectively under-sampled and transformed into image space for the training process. The human training data included both healthy and unhealthy adults, aged 18 to 70 years, recruited from partner hospitals.

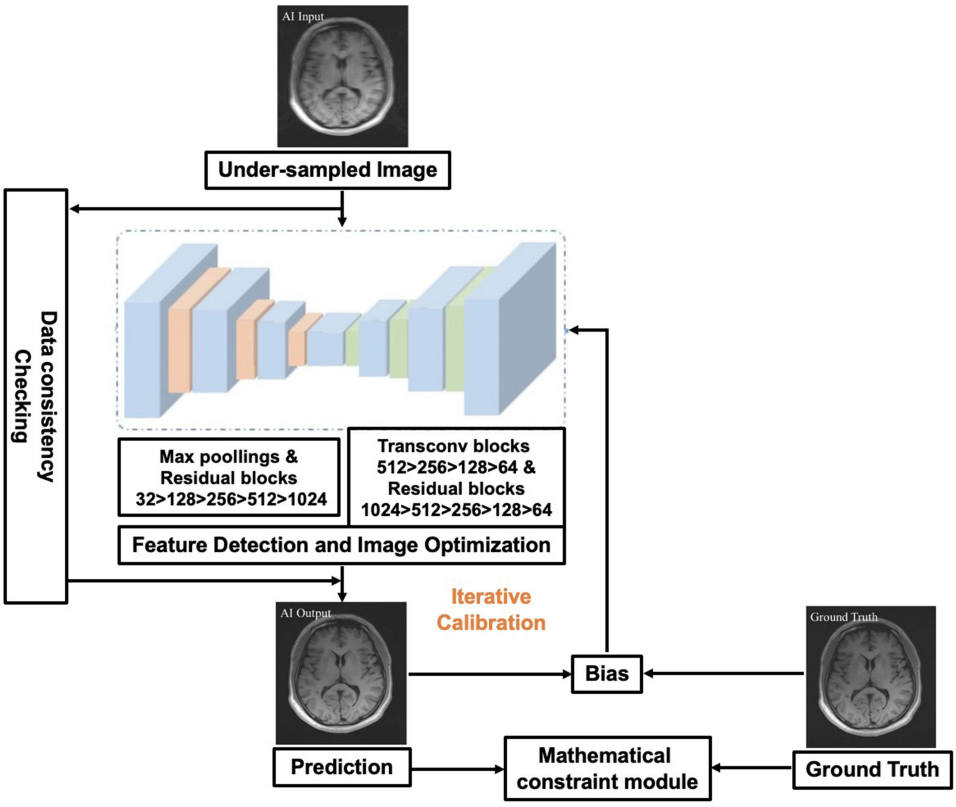

Figure 2 Sketch map of the network design for the artificial intelligence-assisted compressed sensing (ACS).

Image Quality Assessment

Two independent radiologists (WG and CY, with 6 and 5 years of experience, respectively) conducted a blinded, randomized assessment to compare the image quality. They reviewed axial and sagittal T2-weighted images (T2WI) as well as axial FLAIR images from both conventional and ACS protocols, as illustrated in Figure 3. The evaluation of conventional and ACS images was carried out separately, with the order of cases randomized for each assessment. The radiologists, unaware of the clinical details and protocol type, rated the image quality based on avoidance of artifacts, boundary sharpness, visibility of lesions, and overall image quality, utilizing a 5-point Likert scale ranging from 1 ("worst") to 5 ("best"). Each radiologist also measured the signal-to-ratios (SNRs) for various regions, including gray matter (GM), white matter (WM), and cerebrospinal fluid (CSF). They assessed GM/WM contrast noise ratio (CNR) by selecting four circular regions of interest (ROIs), each 3 mm in diameter, within the respective regions. The SNR was calculated by dividing the average signal intensity (SI) of the tissue ROI (SI_{tissue}) by the mean standard deviation (SD) of the background, measured at the four corners (top-left, top-right, bottom-left, and bottom-right) in the same image layer ($SD_{background}$).[23] After obtaining the SNR values, the GM/WM CNR was computed as the difference between the SNRs of GM and WM. Finally, we compared image quality between the conventional and ACS protocols, using both qualitative assessments (artifact avoidance, boundary sharpness, lesion visibility, and overall image quality) and quantitative measures (SNRs and GM/WM contrast).

Diagnostic Assessment

Following the image quality evaluation, the radiologists performed a diagnostic assessment at an individual level, independently identifying pathologies for each participant. They followed the strategies based on established criteria or recommendations.[7,24–26] After completing their individual assessment, the radiologists reviewed the cases with conflicting results and reached a consensus through discussion.

The Fazekas scale (0–3) was applied for assessing white matter hyperintensities (WMH) based on FLAIR images.[7] Specifically, periventricular WMH was graded as follows: 0 = absent, 1 = "caps" or pencil-thin lining, 2 = smooth "halo", and 3 = irregular periventricular hyperintensities (PVH) extending into the deep white matter. Deep WMH were rated as: 0 = absent, 1 = punctate foci, 2 = early confluence of foci, and 3 = large confluent areas. The Fazekas scale was defined by summing the scores of periventricular and deep WMH, with the following classifications: 0 for a sum of 0, 1 for a sum

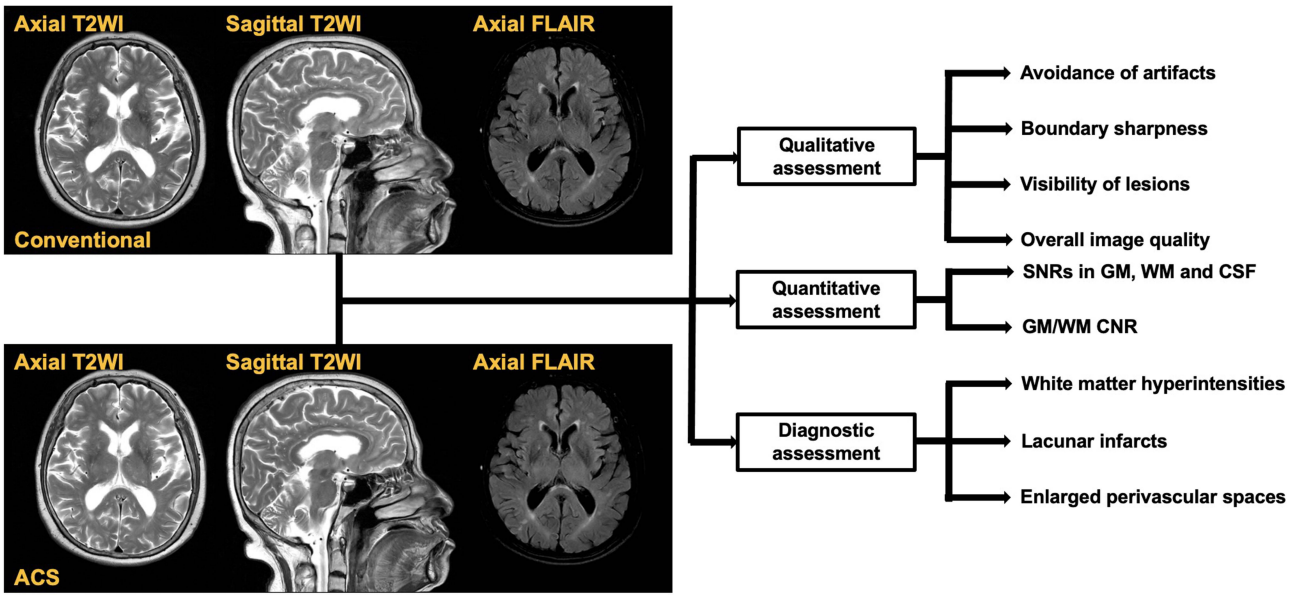

Figure 3 The example and analysis of axial and sagittal T2-weighted (T2WI), and axial T2-fluid attenuated inversion recovery (FLAIR) images, obtained from conventional and ACS protocols.

Abbreviations: ACS, artificial intelligence-assisted compressed sensing; CNR, contrast noise ratio; CSF, cerebrospinal fluid; GM, grey matter, SNR, signal-to-noise ratio, WM, white matter.

https://doi.org/10.2147/IJGM.S499950

of 1 or 2, 2 for a sum of 3 or 4, and 3 for a sum of 5 or 6. Cerebral infarcts were categorized as either territorial or lacunar, utilizing a scoring system based on the number of visible lacunar infarcts on FLAIR images (0 for none, 1 for <= 3, 2 for <= 10, and 3 for > 10).[25] Enlarged perivascular spaces (EPVS) were evaluated separately in the basal ganglia and centrum semiovale, based on axial T2WI. For basal ganglia, EPVS status was graded as 0 (no EPVS), 1 (1–10 EPVS), 2 (11–20 EPVS), 3 (21–30 EPVS) and 4 (>40 EPVS) were applied.[24] For centrum semiovale, EPVS status was graded as 0 (0–10 EPVS) and 1 (>10 EPVS).[24] A total EPVS score was then calculated by adding up the grades from both regions.[24]

Statistical Analysis

To assess the interchangeability of the two imaging protocols, we calculated two types of agreement rates: intra-protocol inter-observer agreement (both observers assessing the conventional protocol images) and inter-protocol inter-observer agreement (one observer evaluating the conventional images and the other evaluating the ACS protocol images) for each variable.[27] We derived the individual equivalence index by subtracting the inter-protocol inter-observer agreement rate from the intra-protocol inter-observer agreement rate. Bootstrapping methods with 1000 repetitions was used to compute the 95% confidence interval (95% CI).[28] Protocols were considered interchangeable if the 95% CI of the individual equivalence index fell below 5%.

Cohen's weighted kappa[29] quantified the inter-protocol intra-observer agreement across all variables and three brain MRI sequences. We also evaluated both the intra-protocol inter-reader agreement (both observers assessing the conventional protocol images) and the inter-protocol inter-reader agreement. The kappa values were interpreted as follows: less than 0.20 for poor agreement, 0.21–0.40 for fair, 0.41–0.60 for moderate, 0.61–0.80 for good, and 0.81–1.00 excellent agreement.

To determine the statistical significance of the differences between the variables from conventional and ACS protocols, we conducted two-tailed t-tests for the continuous variables and chi-squared tests for the discrete ones, respectively. We performed power analysis using the sampsizepwr scripts in MATLAB (MathWorks, Natick, Massachusetts, USA) to ensure adequate sample size. All statistical analyses were performed in MATLAB, with statistical significance set at $p < 0.05$, and Bonferroni correction[30] applied for multiple comparisons.

Results

Participant Characteristics

After enrollment and exclusion, we finally included 70 participants (38 men and 32 women; mean age, 61.6 ± 12.5 years; age range, 50–82 years) in this study. For all the patients included, at least one type of brain MRI abnormalities was found. WMH presented in 60 patients (85.7%, Figure 4), with lesions located in the parietal-occipital lobe (42/60), frontal lobe (40/60), temporal lobe (21/60), basal ganglia (20/60), or infratentorial areas (11/60). Lacunar infarcts were observed in 29 patients (41.4%, Figure 5), primarily in the basal ganglia, coronary radiata, or infratentorial areas. All participants had EPVS (Figure 6), which were found in the basal ganglia (70/70) and centrum semiovale (53/70).

Comparison of Qualitative Assessment

The ACS protocol significantly improved avoidance of artifacts, boundary sharpness, visibility of lesions and overall image quality across all three images types compared to those of the conventional protocol (all $p < 0.001$, after Bonferroni correction, Table 2). Inter-observer agreements, as measured by Cohen's weighted kappa, were good-to-excellent for all evaluated factors: avoidance of artifacts (0.78), boundary sharpness (0.74), visibility of lesions (0.70) and overall image quality (0.86).

Comparison of Quantitative Assessment

The results of SNRs and GM/WM CNR are shown in Table 3. The SNRs in GM and WM, and GM/WM CNR significantly increased in ACS axial T2WIs, compared to conventional ones (all $p < 0.05$, after Bonferroni correction). With the current sample size of 70 participants, the powers of the significant group differences for both qualitative and quantitative assessment exceeded 0.80.

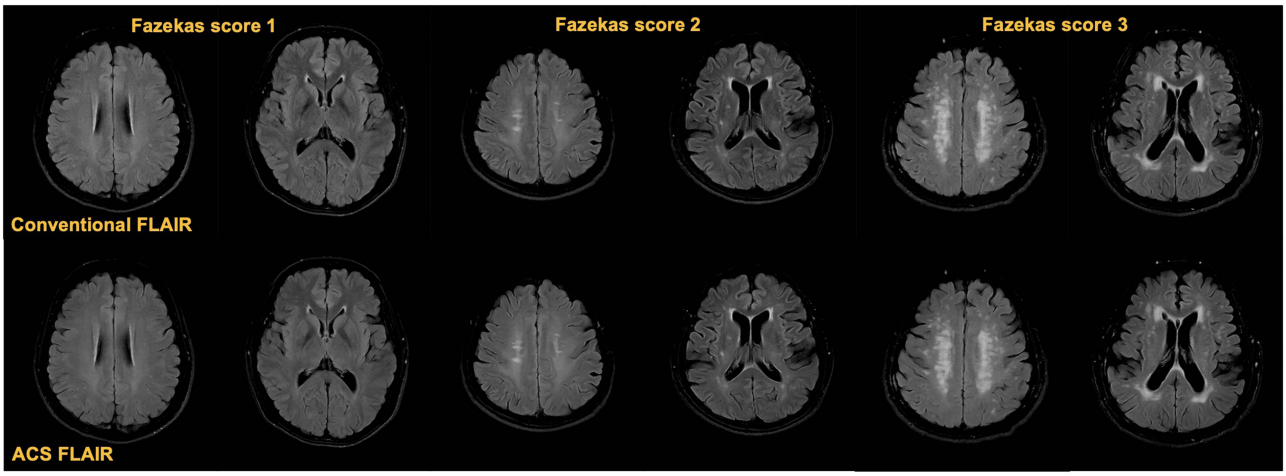

Figure 4 Axial T2-fluid attenuated inversion recovery (FLAIR) images of participants with white matter hyperintensities (Fazekas score 1–3), were obtained from both conventional (upper) and ACS (lower) protocols.
Abbreviation: ACS, artificial intelligence-assisted compressed sensing.

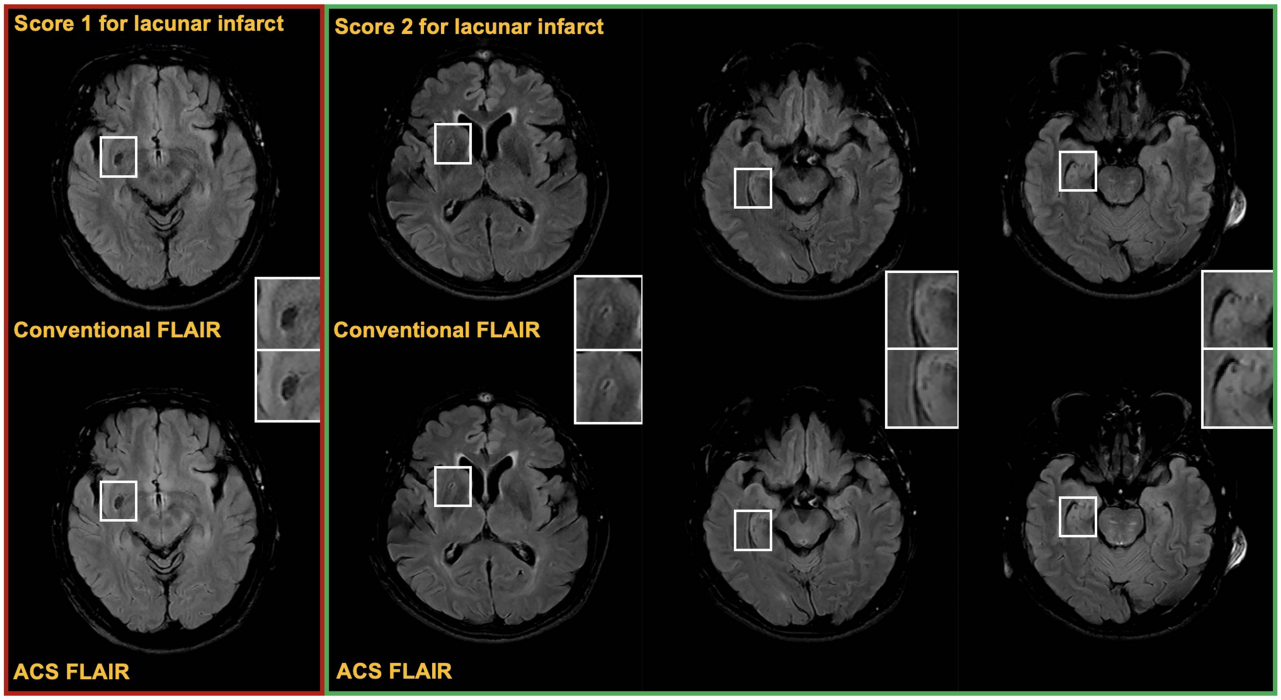

Figure 5 Axial T2-fluid attenuated inversion recovery (FLAIR) images of participants with lacunar infarct (score 1–2), were obtained from both conventional (upper) and ACS (lower) protocols. The regions of lacunar infarct in FLAIR images were indicated with white boxes and amplified in the lower right corners.
Abbreviation: ACS, artificial intelligence-assisted compressed sensing.

Diagnostic Equivalence

A number of cases with different pathologies, including WMH, lacunar infarct and EPVS, are presented in Table 4. There were no significant differences between conventional and ACS MR images in detecting these pathologies (all $p > 0.05$, after Bonferroni correction). Table 4 also shows the kappa values for the inter-protocol intra-observer agreement, intra-protocol (conventional vs conventional) inter-observer agreement, and inter-protocol inter-observer agreement. The inter-protocol intra-observer agreement (kappa values [95% CI]) for evaluating pathologies was excellent for conventional and ACS images: 0.94 [0.92–0.96], 0.89 [0.86–0.92], 0.86 [0.82–0.90], respectively.

https://doi.org/10.2147/IJGM.S499950

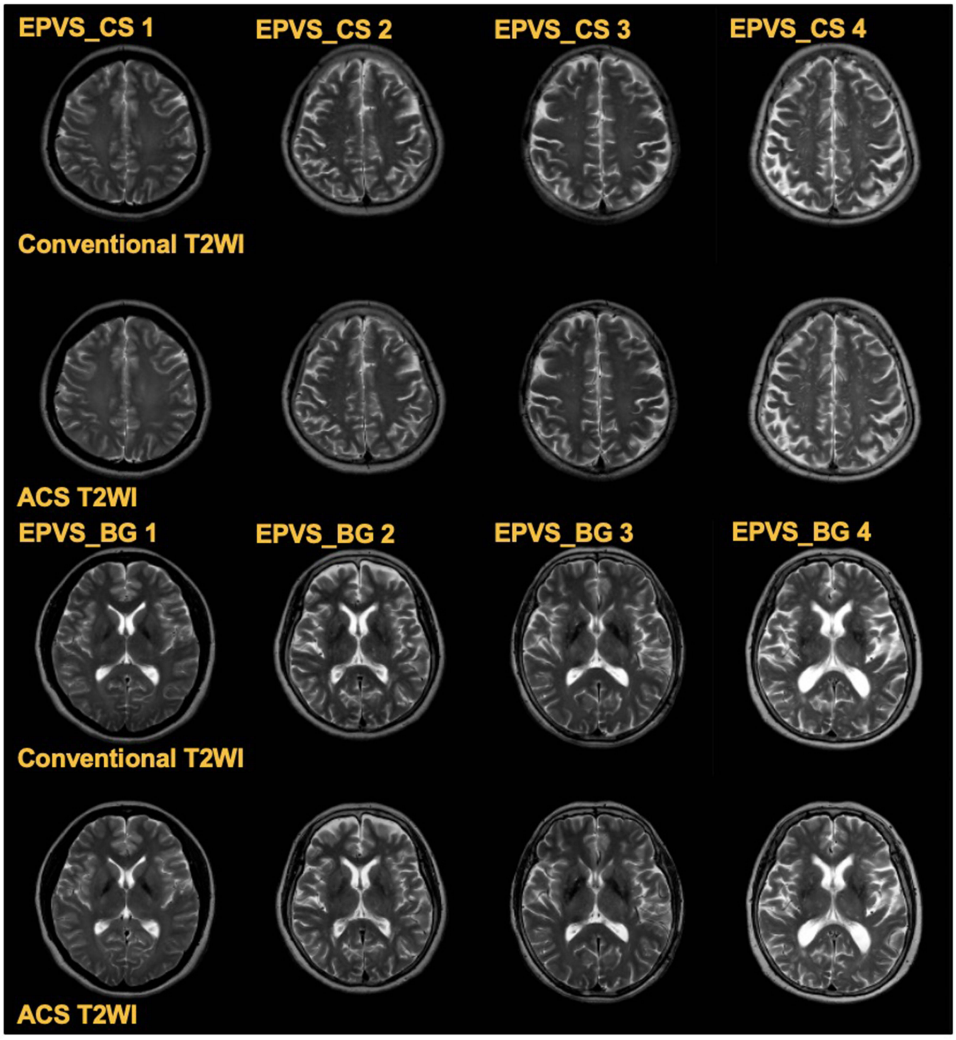

Figure 6 Axial T2-weighted MR images (T2WI) of participants with enlarged perivascular space (EPVS, 1–4), were obtained from both conventional (upper) and ACS (lower) protocols.
Abbreviations: ACS, artificial intelligence-assisted compressed sensing; BG, basal ganglia; CS, centrum semiovale.

Table 5 presents the intra-protocol (conventional vs conventional) inter-observer and inter-protocol inter-observer agreement rates, along with the 95% CIs for the individual equivalence indices. Specifically, for the WMH and lacunar infarct, the highest upper bound of the 95% CI falls within 5%, indicating that the two protocols can be considered interchangeable for these conditions. However, for EPVS, the upper bound of the 95% CI is slightly higher at 5.89%.

Table 2 Qualitative Assessment and Comparison

	Score (1–5)		P-value	Inter-Observer Agreement
	Conventional	ACS		
Avoidance of artifacts	4.06 ± 0.63	4.44 ± 0.90	<0.001*	0.78 (0.74–0.82)
Boundary sharpness	4.01 ± 0.72	4.31 ± 0.77	<0.001*	0.74 (0.71–0.77)
Visibility of lesions	3.84 ± 0.61	4.11 ± 0.80	<0.001*	0.70 (0.66–0.74)
Overall image quality	4.21 ± 0.63	4.55 ± 0.86	<0.001*	0.86 (0.81–0.91)

Notes: Cohen's weighted kappa values (95% confidence interval) for inter-observer agreement are shown. The p values were calculated with two-tailed t-tests, after Bonferroni correction for multiple comparisons. And the symbol (*) indicates being significant.
Abbreviation: ACS, artificial intelligence-assisted compressed sensing.

Table 3 Quantitative Assessment and Comparison

	Measurement		P-value
	Conventional	ACS	
Axial T2-weighted image			
SNR (GM)	78.42 ± 10.21	90.63 ± 11.32	< 0.001*
SNR (WM)	55.54 ± 8.05	64.51 ± 8.03	< 0.001*
SNR (CSF)	266.13 ± 36.42	283.70 ± 34.03	0.081
GM/WM CNR	22.88 ± 5.16	26.12 ± 6.24	0.006*
Sagittal T2-weighted image			
SNR (GM)	86.61 ± 18.68	84.63 ± 14.47	> 0.90
SNR (WM)	65.24 ± 12.53	64.32 ± 12.03	> 0.90
SNR (CSF)	250.59 ± 52.13	258.22 ± 45.30	> 0.90
GM/WM CNR	21.37 ± 10.18	20.31 ± 5.92	> 0.90
Axial T2-FLAIR image			
SNR (GM)	69.82 ± 9.37	71.24 ± 9.81	> 0.90
SNR (WM)	64.70 ± 9.33	69.32 ± 8.06	0.081
SNR (CSF)	10.41 ± 3.93	9.78 ± 3.64	> 0.90
GM/WM CNR	5.12 ± 5.51	1.92 ± 6.32	0.10

Notes: The p values were calculated with two-tailed paired t-tests, after Bonferroni correction for multiple comparisons. And the symbol (*) indicates being significant.
Abbreviations: ACS, artificial intelligence-assisted compressed sensing; CNR, contrast noise ratio; CSF, cerebrospinal fluid; FLAIR, fluid attenuated inversion recovery; GM, grey matter; SNR, signal-to-noise ratio; WM, white matter.

Table 4 Integrated Results of Diagnostic Performance by Two Observers

	Number of Cases		P-value	Inter-Protocol Intra-Observer Agreement	Intra-Protocol Inter-Observer Agreement	Inter-Protocol Inter-Observer Agreement
	Conventional	ACS				
Fazekas score (0/1/2/3)	10/39/14/7	10/39/14/7	> 0.90	0.94 (0.92–0.96)	0.74 (0.70–0.78)	0.76 (0.72–0.80)
Lacunar infarct (0/1/2/3)	41/21/8/0	42/20/8/0	> 0.90	0.89 (0.86–0.92)	0.80 (0.75–0.85)	0.77 (0.72–0.82)
EPVS (0/1/2/3/4/5)	0/6/11/20/17/16	0/6/10/22/16/16	> 0.90	0.86 (0.82–0.90)	0.70 (0.67–0.73)	0.71 (0.66–0.76)

Notes: Cohen's weighted kappa values (95% confidence interval) for agreement evaluation are shown. The p values were calculated with chi-squared tests.
Abbreviations: ACS, artificial intelligence-assisted compressed sensing; EPVS, enlarged perivascular space.

Table 5 Interchangeability Results for Two Protocols

		Inter-Observer Agreement Rate	95% CI of the Individual Equivalence Index (%)
Fazekas score	Intra-protocol	72.9%	−0.76 to 0.61
	Inter-protocol	71.5%	
Lacunar infarct	Intra-protocol	66.5%	−2.42 to 3.51
	Inter-protocol	64.5%	
EPVS	Intra-protocol	86.1%	−0.42 to 5.89
	Inter-protocol	84.8%	

Abbreviations: ACS, artificial intelligence-assisted compressed sensing; CI, confidence interval; EPVS, enlarged perivascular space.

Discussion

Our study evaluated the image quality and diagnostic utility of ACS-accelerated brain MRI protocol compared to the conventional protocol. The accelerated images delivered comparable performance in detecting aging-related cerebral pathologies, matching the diagnostic capability of standard MRI. This finding was reinforced by the robust inter-protocol intra-observer agreement across all assessed features. Therefore, ACS offers a practical and time-efficient option for some routine brain MRI sequences, significantly reducing about 30% scan time without compromising diagnostic accuracy.

A recent study claimed a more-than-half reduction of acquisition time using the same techniques on musculoskeletal system.[31] However, part of this huge saving might be due to a reduction of slice resolution or optimized TR and echo train length, which confounds the true contribution from ACS.[31] This study obeyed the principle of a solid comparison, controlling the sequence parameters. The accelerating parameters were set at a relative conservative level (ACS factor 2.2) to avoid low image fidelity. Higher accelerating factor would further shorten the acquisition, yet possibly at the expense of impaired image quality for accurate diagnosis. Previous work on ankle MRI has illustrates significant blurring artifacts at an accelerating factor of 3.7.[32] Moreover, the impact of specific coil on our results necessitate further investigation.

In our study, ACS images consistently outperformed those obtained through PI in terms of avoidance of artifacts. The inter-observer agreement results confirmed that good-to-excellent consistency in this evaluation. The improved artifact reduction likely resulted from the shorter scan durations, which minimized patient movement. Previous studies have illustrated the potential of CS accelerated brain MRI protocols bringing a near thirty-percentage time saving.[12] However, special related artefacts were reported as a limitation of CS, including the wax-layer artefact and streaky-linear ones.[33,34] In this study, no such artefacts were not observed. By incorporating deep learning pre-trained reconstruction, AI-assisted CS should in principle perform better in artefact control.[35] By learning to remove noise and suppress artifacts, ACS trained on a huge dataset of fully sampled images seems to prevent the typical degradation seen in conventional accelerating methods. Yet, the optimistic conclusion of reduced artefacts still deserve further validation: current ACS applications are only available on 2D sequences, while indeed 3D sequences are more addressed on this topic.[33] In qualitative assessment, margin sharpness of lesions was clearer in ACS images, aiding in the diagnosis of small pathological such as lacunar infarcts or EPVS. These slightly higher qualitative scores are indeed not in expectation before the study, and may only be explained by the assistance of deep learning reconstruction using high-quality training data. Similarly, a previous study reported better performance of deep-learning reconstructed FLAIR brain imaging in image quality as well as achieving additional reduction in examination time.[36]

The quantitative assessment showed that when applying ACS and PI with the same parameters on the same patient, ACS images had similar or higher SNR and CNR values compared to conventional ones using PI, despite difference in scan time. This suggests that ACS effectively maintained the imaging details of the human brain. The filtering and interpolation, powered by convolutional neural networks, achieve high-resolution imaging without loss of time or SNR. This capability allows ACS to produce at least equivalent image quality across various body regions, including brain and spine,[22,37] joint,[31,32,38] heart[39] and abdomen.[18,19] Yet, a slight loss of white matter/grey matter CNR was observed on FLAIR images, although not significant. Fortunately, this loss of CNR did not affects the detectability of WMH due to their higher signal intensities than normal white matter.

For elderly individuals, common pathologies such as WMH, lacunar infarct and EPVS require regular monitoring, particularly in community hospitals. Thus, maintaining diagnostic accuracy and efficiency is essential for routine brain MRI. Our findings suggest that ACS optimizes clinical workflow without compromising diagnostic information. Unlike the previous study focused on normal structures,[21] our study demonstrates that ACS preserves pathological information in brain MR images. These findings align with recent studies showing that AI-based accelerated imaging techniques enhance the visualization of pathologies without sacrificing diagnostic quality.[22,36]

We acknowledge several limitations in our study. First, ACS is not yet available for 3D sequences, so geometric measurements on cerebral 3D T1-weighted images were not included. These measurements are clinically relevant, especially in elderly patients. Second, the study focused on a small, specialized patient cohort and relied on a single 3.0 Tesla MRI scanner from one manufacturer, which may limit the generalizability of our findings. Future research should

aim to include larger, more diverse cohorts and validate the results across different scanner models to confirm the broader applicability and clinical utility of AI-based accelerated imaging techniques. Additionally, we did not compare different acceleration factors, which could provide valuable insights into the trade-off between scan time reduction and image fidelity. The acceleration factor of 2.2, as recommended by the manufacturer for routine brain MRI, was used in this study. Given the limited scan times for elderly patients, we focused on comparing ACS protocols at this setting with conventional protocols. Further studies should explore the impact of varying acceleration factors on image quality and diagnostic accuracy, particularly in younger populations.

Conclusion

Our study provides evidence that the T2-weighted brain MRI protocol utilizing the ACS acceleration technique delivers at least equivalent results to the conventional protocol with parallel imaging with an approximate thirty-percentage time saving across image quality and diagnostic assessment. This indicates the usefulness of ACS in MRI for aging-related cerebral disease, especially for those community hospitals or low-or-middle income countries with constrained resources.

Acknowledgments

The authors thank all the subjects who participated in this study.

Funding

This work was supported by Specialty Feature Construction Project of Health Commission of Pudong New District, Shanghai, China [Grant No. PWZzb2022-18].

Disclosure

The authors report no conflicts of interest in this work.

References

1. Brayne C. The elephant in the room - healthy brains in later life, epidemiology and public health. *Nat Rev Neurosci*. 2007;8(3):233–239. doi:10.1038/nrn2091
2. Hagiwara A, Takahashi M. Advanced techniques for MR neuroimaging. *Magn Reson Med Sci*. 2024;23(3):249–251. doi:10.2463/mrms.e.2024-1000
3. Kazmierczak PM, Duhrsen M, Forbrig R, et al. Ultrafast brain magnetic resonance imaging in acute neurological emergencies: diagnostic accuracy and impact on patient management. *Invest Radiol*. 2020;55(3):181–189. doi:10.1097/RLI.0000000000000625
4. Runge VM, Aoki S, Bradley WG Jr, et al. Magnetic resonance imaging and computed tomography of the brain-50 years of innovation, with a focus on the future. *Invest Radiol*. 2015;50(9):551–556. doi:10.1097/RLI.0000000000000170
5. Pantoni L. Cerebral small vessel disease: from pathogenesis and clinical characteristics to therapeutic challenges. *Lancet Neurol*. 2010;9(7):689–701. doi:10.1016/S1474-4422(10)70104-6
6. Filippi M, Preziosa P, Banwell BL, et al. Assessment of lesions on magnetic resonance imaging in multiple sclerosis: practical guidelines. *Brain*. 2019;142:1858–1875. doi:10.1093/brain/awz144
7. Fazekas F, Chawluk JB, Alavi A, Hurtig HI, Zimmerman RA. MR signal abnormalities at 1.5 T in Alzheimer's dementia and normal aging. *AJR Am J Roentgenol*. 1987;149(2):351–356. doi:10.2214/ajr.149.2.351
8. Zaitsev M, Maclaren J, Herbst M. Motion artifacts in MRI: a complex problem with many partial solutions. *J Magn Reson Imaging*. 2015;42(4):887–901. doi:10.1002/jmri.24850
9. Andre JB, Bresnahan BW, Mossa-Basha M, et al. Toward quantifying the prevalence, severity, and cost associated with patient motion during clinical MR examinations. *J Am Coll Radiol*. 2015;12(7):689–695. doi:10.1016/j.jacr.2015.03.007
10. Dieckmeyer M, Roy AG, Senapati J, et al. Effect of MRI acquisition acceleration via compressed sensing and parallel imaging on brain volumetry. *MAGMA*. 2021;34(4):487–497. doi:10.1007/s10334-020-00906-9
11. Larkman DJ, Nunes RG. Parallel magnetic resonance imaging. *Phys Med Biol*. 2007;52(7):R15–55. doi:10.1088/0031-9155/52/7/R01
12. Monch S, Sollmann N, Hock A, Zimmer C, Kirschke JS, Hedderich DM. Magnetic resonance imaging of the brain using compressed sensing - quality assessment in daily clinical routine. *Clin Neuroradiol*. 2020;30(2):279–286. doi:10.1007/s00062-019-00789-x
13. Lustig M, Donoho D, Pauly JM. Sparse MRI: the application of compressed sensing for rapid MR imaging. *Magn Reson Med*. 2007;58(6):1182–1195. doi:10.1002/mrm.21391
14. Vranic JE, Cross NM, Wang Y, Hippe DS, de Weerdt E, Mossa-Basha M. Compressed Sensing-Sensitivity Encoding (CS-SENSE) accelerated brain imaging: reduced scan time without reduced image quality. *AJNR Am J Neuroradiol*. 2019;40(1):92–98. doi:10.3174/ajnr.A5905
15. Kanemaru N, Takao H, Amemiya S, Abe O. The effect of a post-scan processing denoising system on image quality and morphometric analysis. *J Neuroradiol*. 2022;49(2):205–212. doi:10.1016/j.neurad.2021.11.007
16. Knoll F, Murrell T, Sriram A, et al. Advancing machine learning for MR image reconstruction with an open competition: overview of the 2019 fastMRI challenge. *Magn Reson Med*. 2020;84(6):3054–3070. doi:10.1002/mrm.28338

17. Wang S, Cao G, Wang Y, et al. Review and prospect: artificial intelligence in advanced medical imaging. *Front Radiol*. 2021;1:781868. doi:10.3389/fradi.2021.781868
18. Sheng RF, Zheng LY, Jin KP, et al. Single-breath-hold T2WI liver MRI with deep learning-based reconstruction: a clinical feasibility study in comparison to conventional multi-breath-hold T2WI liver MRI. *Magn Reson Imaging*. 2021;81:75–81. doi:10.1016/j.mri.2021.06.014
19. Zhao Y, Peng C, Wang S, Liang X, Meng X. The feasibility investigation of AI -assisted compressed sensing in kidney MR imaging: an ultra-fast T2WI imaging technology. *BMC Med Imaging*. 2022;22(1):119. doi:10.1186/s12880-022-00842-1
20. Gu J, Wang Z, Kuen J, et al. Recent advances in convolutional neural networks. *Pattern Recognit*. 2015;77:354–377. doi:10.1016/j.patcog.2017.10.013
21. Karthik A, Aggarwal K, Kapoor A, et al. Comprehensive assessment of imaging quality of artificial intelligence-assisted compressed sensing-based MR images in routine clinical settings. *BMC Med Imaging*. 2024;24(1):284. doi:10.1186/s12880-024-01463-6
22. Liu H, Deng D, Zeng W, et al. AI-assisted compressed sensing and parallel imaging sequences for MRI of patients with nasopharyngeal carcinoma: comparison of their capabilities in terms of examination time and image quality. *Eur Radiol*. 2023;33(11):7686–7696. doi:10.1007/s00330-023-09742-6
23. Goerner FL, Clarke GD. Measuring signal-to-noise ratio in partially parallel imaging MRI. *Med Phys*. 2011;38(9):5049–5057. doi:10.1118/1.3618730
24. Doubal FN, MacLullich AM, Ferguson KJ, Dennis MS, Wardlaw JM. Enlarged perivascular spaces on MRI are a feature of cerebral small vessel disease. *Stroke*. 2010;41(3):450–454. doi:10.1161/STROKEAHA.109.564914
25. Vemuri P, Decarli C, Duering M. Imaging markers of vascular brain health: quantification, clinical implications, and future directions. *Stroke*. 2022;53(2):416–426. doi:10.1161/STROKEAHA.120.032611
26. Wahlund LO, Barkhof F, Fazekas F, et al. A new rating scale for age-related white matter changes applicable to MRI and CT. *Stroke*. 2001;32(6):1318–1322. doi:10.1161/01.str.32.6.1318
27. Obuchowski NA, Subhas N, Schoenhagen P. Testing for interchangeability of imaging tests. *Acad Radiol*. 2014;21(11):1483–1489. doi:10.1016/j.acra.2014.07.004
28. Campbell MK, Torgerson DJ. Bootstrapping: estimating confidence intervals for cost-effectiveness ratios. *QJM*. 1999;92(3):177–182. doi:10.1093/qjmed/92.3.177
29. Marasini D, Quatto P, Ripamonti E. Assessing the inter-rater agreement for ordinal data through weighted indexes. *Stat Methods Med Res*. 2016;25(6):2611–2633. doi:10.1177/0962280214529560
30. Armstrong RA. When to use the Bonferroni correction. *Ophthalmic Physiol Opt*. 2014;34(5):502–508. doi:10.1111/opo.12131
31. Wang Q, Zhao W, Xing X, et al. Feasibility of AI-assisted compressed sensing protocols in knee MR imaging: a prospective multi-reader study. *Eur Radiol*. 2023;33(12):8585–8596. doi:10.1007/s00330-023-09823-6
32. Zhao Q, Xu J, Yang YX, et al. AI-assisted accelerated MRI of the ankle: clinical practice assessment. *Eur Radiol Exp*. 2023;7(1):62. doi:10.1186/s41747-023-00374-5
33. Sartoretti T, Reischauer C, Sartoretti E, Binkert C, Najafi A, Sartoretti-Schefer S. Common artefacts encountered on images acquired with combined compressed sensing and SENSE. *Insights Imaging*. 2018;9(6):1107–1115. doi:10.1007/s13244-018-0668-4
34. Meister RL, Groth M, Zhang S, Buhk JH, Herrmann J. Evaluation of artifact appearance and burden in pediatric brain tumor MR imaging with compressed sensing in comparison to conventional parallel imaging acceleration. *J Clin Med*. 2023;12(17):5732. doi:10.3390/jcm12175732
35. Yang G, Yu S, Dong H, et al. DAGAN: deep De-Aliasing generative adversarial networks for fast compressed sensing MRI reconstruction. *IEEE Trans Med Imaging*. 2018;37(6):1310–1321. doi:10.1109/TMI.2017.2785879
36. Estler A, Hauser TK, Mengel A, et al. Deep learning accelerated image reconstruction of fluid-attenuated inversion recovery sequence in brain imaging: reduction of acquisition time and improvement of image quality. *Acad Radiol*. 2024;31(1):180–186. doi:10.1016/j.acra.2023.05.010
37. Sui H, Gong Y, Liu L, et al. Comparison of Artificial Intelligence-Assisted Compressed Sensing (ACS) and routine two-dimensional sequences on lumbar spine imaging. *J Pain Res*. 2023;16:257–267. doi:10.2147/JPR.S388219
38. Liu J, Li W, Li Z, et al. Magnetic resonance shoulder imaging using deep learning-based algorithm. *Eur Radiol*. 2023;33(7):4864–4874. doi:10.1007/s00330-023-09470-x
39. Yan X, Ran L, Zou L, et al. Dark blood T2-weighted imaging of the human heart with AI-assisted compressed sensing: a patient cohort study. *Quant Imaging Med Surg*. 2023;13(3):1699–1710. doi:10.21037/qims-22-607